Spatial relationship between the field-measured ambient gamma dose equivalent rate and geological conditions in a granitic area, Velence Hills, Hungary: An application of digital spatial analysis methods

Silvana Beltrán Torres[a], Attila Petrik[b], Katalin Zsuzsanna Szabó[c,*], Gyozo Jordan[d,e], Jun Yao[f], Csaba Szabó[a]

[a] Lithosphere Fluid Research Laboratory, Department of Petrology and Geochemistry, Eötvös Loránd University, Pázmány Péter sétány 1/C, 1117, Budapest, Hungary
[b] Department of Earth, Environment and Resources Sciences, University of Naples Federico II, Via Cintia snc, 80126, Naples, Italy
[c] Department of Chemistry, Szent István University, Páter Károly utca 1, 2103, Gödöllő, Hungary
[d] Department of Applied Chemistry, Szent István University, Villányi út 35-43, 1118, Budapest, Hungary
[e] State Key Laboratory for Environmental Geochemistry, China Academy of Sciences, 550081, 99 Linchengxi Road, Guiyang, Guizhou, China
[f] Institute for Earth Sciences, China University of Geosciences (Beijing), No. 29, Xueyuan Road, Haidian District, Beijing, China

ARTICLE INFO

In order to estimate the annual dose that the public receive from natural radioactivity, the identification of the potential risk areas is required which, in turn, necessitates understanding the relationship between the spatial distribution of natural radioactivity and the geogenic risk factors (e.g., rock types, presence of dikes, faults, physical conditions of soil, etc.). A detailed spatial analysis of outdoor ambient gamma dose equivalent rate was performed in the western side of Velence Hills, the largest outcropped granitic area in Hungary. In order to assess the role of local geology in the spatial distribution of gamma dose rates, field measurements were carried out at ground level at 300 sites along a 250 m x 250 m regular grid in a total surface of 19.8 km^2. Digital image processing methods were applied to identify anomalies, heterogeneities and spatial patterns in the measured gamma dose rates, including local maxima and minima determination, digital cross sections, gradient magnitude and gradient direction, second derivative profile curvature, local variability, lineament density, 2D auto-correlation and directional variogram analyses. Statistical inference shows that different gamma dose rate levels are associated with the geological formations, with the highest level on the Carboniferous granite including outlying values. Moreover, digital image processing reveals that linear gamma dose rate spatial features are parallel to the SW-NE dike system and to the NW-SE main fractures. The results of this study underline the importance of understanding the role of geogenic risk factors influencing the ambient gamma dose equivalent rate received by public. The study also demonstrates the power of the image processing techniques for the identification of spatial pattern in field-measured geogenic radiation.

1. Introduction

Approximately 84% of the 2.4 mSv effective dose, which humans receive per year, comes from terrestrial, whereas the remaining 16% comes from cosmic sources (UNSCEAR, 2000). Terrestrial natural radioactivity levels vary according to geological features since its source is the earth materials. It is important to identify areas where natural radiation is elevated which necessitates understanding the relationship between the spatial distribution of natural radioactivity and the geogenic factors such as rock type, tectonic fractures and special geological features such as dikes or karst systems. As an example, the

European Atlas of Natural Radiation, which has been under development since 2006, will be a collection of maps including terrestrial gamma dose rate, which in turn requires the understanding of the underlying geological condition (Cinelli et al., 2015; De Cort et al., 2011). Also, terrestrial gamma dose rate can use as a predictor of the radon flux or geogenic radon potential (Bossew et al., 2015a; b; Cinelli et al., 2015; Manohar et al., 2013; Szegvary et al., 2007). Quindós et al. (2008) tested the usability of gamma dose rate for prediction indoor radon levels in a granitic region. They concluded, based on their investigations at three different gamma radiation levels ($< 87\,\mathrm{nGy\,h^{-1}}$, $87\text{–}130\,\mathrm{nGy\,h^{-1}}$, and $> 130\,\mathrm{nGy\,h^{-1}}$), that gamma dose rate is a

* Corresponding author.
  E-mail address: sz_k_zs@yahoo.de (K.Z. Szabó).

qualitative indicator of high indoor radon level rather than a good quantitative predictor. External gamma dose rate has been proved to discriminate non-radon-prone municipalities by García-Talavera et al. (2013) based on studies on 14 different lithostratigraphic units.

The most common field measured quantity of natural background radiation is the ambient dose equivalent rate, H*(10), in units of milliSievert per hour (mSv h^{-1}), which is a measurable equivalent of the above mentioned effective dose, quantifying the risk to human health associated with the radiation exposure (ICRU-51, 1993). However, the measured ambient dose rate, H*(10), consists of several artificial and natural components described by Szabó et al. (2017), and there are methods to distinguish the natural terrestrial component (Bossew et al., 2017).

Basic spatial analysis methods (i.e. ordinary and universal kriging) are frequently applied for natural radioactivity data (for instance, gamma-radiation) which is commonly related to the geological background using statistical methods (García-Talavera et al., 2013; Hiemstra et al., 2009; Manohar et al., 2013; Ramli et al., 2001; Sanusi et al., 2014; Yeşilkanat et al., 2015). Advanced spatial analysis (i.e. digital image processing) revealed spatial relationship between soil gas radon activity concentration, geogenic radon potential and ambient dose rate, and geological and geomorphological features (Szabó et al., 2014, 2017). In these studies, main spatial features, identified in the soil gas radon activity concentration, geogenic radon potential and ambient dose rate are influenced by the underlying geological structures and surface sediment distribution defined by morphological conditions in the study area. However, there are still very few examples for the application of advanced digital spatial analysis methods such as digital image processing for investigating gamma dose equivalent rate spatial pattern and its possible link to underlying geological structures, as demonstrated in the present study.

The main objective of this study is investigating the relationship between the field-measured gamma dose rate and the underlying geology (rock type, dikes, fractures, topography) through the application of digital spatial pattern analysis. Elevated radiation levels generally are associated with igneous rocks, such as granite, and lower levels with sedimentary rocks (UNSCEAR, 2000). Accordingly, an extensive field campaign was carried out and a detailed spatial analysis of the measured ambient gamma dose equivalent rate was performed in the western side of the Velence Hills granitic area in Hungary. Digital spatial analysis methods were applied to the measured data in order to identify spatial patten such as anomalies, heterogeneities and linear features. The identified features were then related to the underlying bedrock lithology and geological structures such as faults and dikes by means of GIS spatial analysis techniques and statistical correlation analysis. This research examines the spatial relationship between field measured gamma dose equivalent rate and observed dike density, fault density and the variability of topographic terrain for the first time.

2. Study area

The 19.8 km^2 study area is located in the western side of the Velence Hills, about 50 km southwest from Budapest (Fig. 1A). The Velence Hills main mass is made up by the outcropping Velence Granite Formation that was formed in the Variscan orogeny in the Carboniferous (280–300 Ma). Subaerial redeposited clastic sediments of Neogene with Pannonian age (8.9–5.33 Ma), are found inside and at the edges of the study area (Buda, 1981; Horváth et al., 2004) (Fig. 1B). Flat areas, valley bottoms and hill slopes are sporadically covered by Pleistocene and Holocene sediments such as loess, sand, proluvial, deluvial and eolic sediments and fluvial and peat deposits (Fig. 1B).

In the granitic outcrop a dike complex was formed in different geological times having a predominant SW-NE strike (Buda, 1981; Horváth et al., 2004). Based on the mineralogical composition, three types of dikes can be identified in the study area: granite porphyry, quartz and monchiquite dikes. The first one, the most abundant in the

study area was formed in the late phase of the granite intrusion, showing slight chemical difference compared to granite (Horváth et al., 2004; Benkó et al., 2014). Quartz dikes are originated by a hydrothermal activity, associated also to the granite formation (Horváth et al., 2004; Benkó et al., 2014) and their age is unknown (Horváth et al., 2004). Monchiquite dikes crystallized from a volatile rich mafic melt in the late Cretaceous (Horváth et al., 2004) (Fig. 1B). Only three 30–70 cm thick mochiquite dikes were mapped in the study area (Gyalog and Horváth, 1999; Horváth et al., 2004). Such dikes are highly enriched in U (up to 10 ppm) and Th (up to 140 ppm) in the wider region (Szabó et al., 1993), whereas the Velence Hills granite shows a range of 2.5–5.4 ppm for U and 16.9–23.3 ppm for Th (Burján et al., 2002). According to Horváth et al. (2004) and Benkó et al. (2014), the main orientation of fractures in the granite is SE-NW, perpendicular to granite porphyry dikes orientation, and they dissect the hills along valleys and streamlets. In contrast, the orientation of the less abundant dikes, quartz and monchiquite, is mainly NS (Horváth et al., 2004) (Fig. 1B and see Fig. 10).

The study area in the Velence Hills is dominated by forest and grasslands and includes the village Pákozd with > 3000 inhabitants. The topographic elevation varies between 110 and 241 m above the sea level (Fig. 1A). The climate is temperate continental with a mean of annual temperature around 10 °C and average of 550–600 mm of annual precipitation (Mezősi, 2015). The geological information for this study is based on the 1:25,000 scale map of the Velence hills compiled by Gyalog and Horváth (1999).

3. Materials and methods

3.1. Field measurement

Ambient gamma dose equivalent rate (H*(10)) was measured in situ by FH 40 G-L10 instrument (Thermo Fisher Scientific Inc.). Measuring range of the energy filtered proportional counter tube gamma detector is 10 nSv h^{-1} -100 mSv h^{-1} and its energy range is 30 keV - 4.4 MeV. The measurements were performed at the standard heights of 1 m and 0 m above the surface. Gamma dose rate of each site was calculated by averaging 3–6 values recorded each minute.

Measurement error was characterized by first calculating the average and standard deviation from the 3–6 measurements for each site that yielded 300 average and 300 standard deviation values. Then, the minimum, maximum and the average of the 300 standard deviation values were found (Table 1). The standard deviation, on average, remains within the 10% of the total average value, which is an acceptable uncertainty for the purpose of this study (Table 1). A grid based sampling strategy was applied. Gamma dose rate was measured at 300 sites along a 250 × 250 m grid over the 19.8 km^2 study area (Fig. 1). Inaccessible sites were measured at the closest points. The survey focused on the granite outcrop area (Fig. 1B): 53% (160 sites) and 47% (140 sites) of the measured sites were located on the granite and other formations, respectively (Fig. 1B). The measurements were carried out during June and July in 2016, under similar field conditions. In addition, temperature, relative humidity and pressure were also measured at each site.

3.2. Statistical analysis

Central tendency and variability measures of the gamma dose rate used in this study were minimum, average (arithmetic mean), median, maximum, standard deviation, median absolute deviation (MAD) and range. For outlier identification Tukey (1977) inner fence criteria was used. Normality of the distributions was tested by the Chi-square test and the Kolmogorov-Smirnov test. The Mann-Whitney (Wilcoxon) homogeneity test was used to compare the median of gamma dose rate values measured over various geological rock types and ages (Mann and Whitney, 1947). Bivariate least squares regressional analysis was used
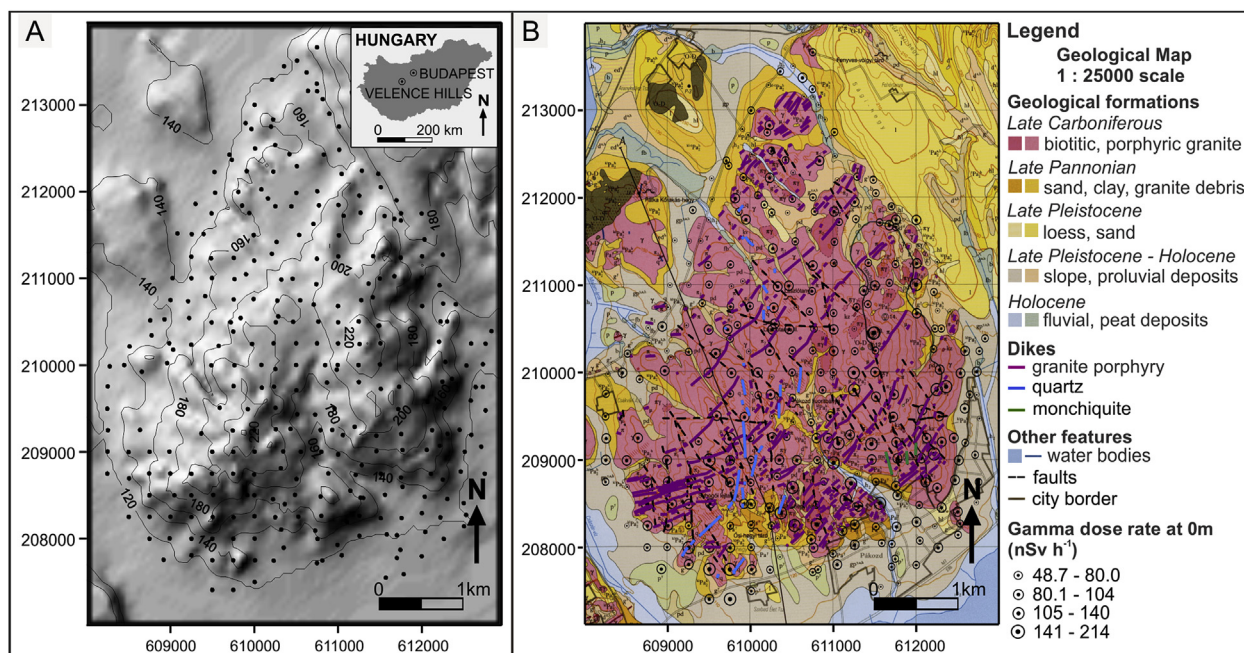
Fig. 1. The Velence Hills study area. A. Topographic shaded relief model with the elevation contour lines overlaid. Figures show elevation above sea level in meters. Solid dots: location of gamma dose rate measurements. Inset: Location of the study area. B. Geological map (scale 1:25,000 after Horváth et al., 2004) overlayed by the fault lines and dikes. The radii of the circles are proportional to the gamma dose rate value (nSv h^{-1}) at the 300 measurement sites. Solid line polygon delineates village Pákozd.

Table 1
Measurement error description. Statistics of the standard deviation calculated from 3 to 6 gamma dose rate measurements at the 300 sites. The related average gamma dose rate values are in the second colourman.

	Standard deviation of gamma dose rate calculated from 3 to 6 measurements at each site (nSv h^{-1})	Related average gamma dose rate calculated from 3 to 6 measurements (nSv h^{-1})
	at 0 m	
minimum	0.2 (n = 300)	80.5 (n = 1)
maximum	42.8 (n = 300)	146.3 (n = 1)
average	10.3 (n = 300)	102.5 (n = 300)
	at 1 m	
minimum	0.5 (n = 300)	76.4 (n = 1)
maximum	43.3 (n = 300)	206.6 (n = 1)
average	9.3 (n = 300)	94.6 (n = 300)

to explore the linear relationship between the measured gamma dose rate and the calculated spatial parameters such as dike density in given areas. Strength of relationship was expressed by the Pearson's correlation coefficient r (Rodgers and Nicewander, 1988). Statistical significance of the fitted linear model was tested by the F-test and its associated P-value (p). A small p value (less than 0.05 since operating at the 5% significance level) indicates that a significant relationship of the form specified exists between Y and X. All of the statistical tests applied in this study were significant at the 95% confidence level.

3.3. Mapping and spatial analysis

Field measured gamma dose rates were interpolated using the triangular irregulation network (TIN) method. TIN is an accurate, linear interpolator honoring the original measurement values and does not require preliminary structural analysis unlike kriging, for example (Guibas and Stolfi, 1985). TIN represents the modelled surface well, especially in the case of regularly located data points (Davis, 2011). The grid size (10 × 10 m) was determined by the shortest distance between measurement points. The TIN interpolated gamma dose rates map was

smoothed with a low-pass moving average filter of increasing window sizes (5 × 5, 7 × 7, 9 × 9, 11 × 11, 13 × 13, 15 × 15, 17 × 17, 19 × 19) to suppress high frequency noise and enhance large scale spatial pattern. The 17 × 17 (170 × 170 m) window size revealed the best the spatial trend and pattern without losing much detail, by visual inspection. Since the objective of this study is to analyse the main spatial patterns without the small scale irregularities, the outlier free TIN interpolated gamma dose rates map was used for digital image processing analysis.

Error of interpolation was estimated by calculating the difference between the interpolated surface and the original data points. Results show that the applied smoothed TIN interpolation is a good model as the average error is -1.21 nSv h^{-1}, equal to a 1.3% relative error, with unbiased symmetric distribution. The *t*-test confirmed that the expected average error is zero at the 95% confidence level. The outlier free data set has a lower average error of -0.75 nSv h^{-1}, equal to a 0.8% relative error. At the few (10) outlier values in the main linear zone anomaly (see below) the error can be as high as -47 and 76 nSv h^{-1}, which confirms the efficiency of the applied smoothing for regional trend pattern recovery.

A systematic digital image processing methodology is applied to the outlier free TIN interpolated gamma dose rates map according to Evans (1972) method as extended by Jordan et al. (2005) and Jordan (2007). This method, originally developed for digital elevation models, proceeds from simple univariate data display and evaluation, through edge detection and image segmentation, to the multivariate interpretation of results using GIS technology.

Shaded relief models were calculated at an azimuth interval of 45° and constant insolation inclination of 45°. The models used Lambertian reflection method and ten time vertical exaggeration. Hill shading increases the contrast of very subtle intensity variations of an image, much more than contouring or pseudocolor representation does (Burrough, 1986; Drury, 1987).

The identification of surface specific points including local maxima (peaks), minima (pits), saddle points (passes), flats and slope breaks is straightforward in digital spatial analysis (Jordan, 2007; Takahashi et al., 1995). Pits and peaks reveal anomalous gamma dose rates and

Table 2
Summary statistics of the ambient gamma dose equivalent rate measured at the 300 sites.

	Count	Minimum (nSv h^{-1})	Maximum (nSv h^{-1})	Range (nSv h^{-1})	Average (nSv h^{-1})	Standard deviation (nSv h^{-1})	Relative variability (%)	Median (nSv h^{-1})	MAD (nSv h^{-1})
at 0 m	300	48.7	214.3	165.6	102.5	27.5	27	100.0	16.9
at 1 m	300	48.5	206.6	158.1	94.6	21.7	23	91.3	13.4

they were calculated by the simple 'higher than' algorithms (Garbrecht and Martz, 1995). Digital cross-sections were made on the TIN interpolated outlier free gamma dose rate map in parallel and perpendicular to the orientation of dikes to capture spatial trends. Dike density map was calculated by using total length of all dikes, regardless of their origin, within a predefined circle of 500 m radius in order to highlight possible spatial relationship between gamma dose rates and dike density. Local variability of gamma dose rates was generated by two different methods. Relief map was calculated on the outlier free gamma dose rate data within increasing window sizes (21 × 21, 41 × 41, 61 × 61, 81 × 81, 101 × 101, 121 × 121 and 141 × 141) by using the range divided by the median value of the gamma dose rates.

Variability index was calculated by taking the square root of the absolute value of the squared differences between the maximum and minimum of gamma dose rate within a pre-defined window size (in this study: 21 × 21, 41 × 41, 61 × 61, 81 × 81, 101 × 101, 121 × 121 and 141 × 141). For both methods, the 101 × 101 (1010 × 1010 m) window size proved to be the best to reveal distinct patterns of local variance. Relief and variability index maps were later smoothed with 41 × 41 (410 × 410 m) and 31 × 31 (310 × 310 m) moving average low pass filters, respectively, to enhance the main spatial pattern of different variability zones. Relief and variability index maps (see Fig. 6A and B) were overlain by all dikes to see whether high dike density corresponds to high local variability of the gamma dose rates.

Two dimensional autocorrelogram was used to identify anisotropy present in the spatial gamma dose rate data. Empirical directional variograms were also calculated in different directions using 30° tolerance angle to reveal anisotropy in the gamma dose rates.

The interpolated gamma dose rate map is a continuous surface of bivariate function and can be analysed for the gradient magnitude ('slope') and gradient direction ('aspect'). These parameters were calculated using the Prewitt-operator, which is an unweighted eight point numerical differentiation method, for its smoothing effect (Gonzalez and Woods, 1993). These gradient calculations were suitable to identify the largest change of the gamma dose rates ('slope') and its direction ('aspect') at each grid point. Uniform aspect with high gradient magnitudes along linear features may indicate geological influence on the gamma dose rates distribution. Profile curvature is the 2nd derivative of gamma dose rates indicating sudden change in gradient magnitude and identifies inflection lines between convex (negative curvature values) and concave (positive curvature values) areas. Classification of gradient or curvature values was performed by using the 'natural break' histogram slicing method at the inflection points on the cumulative distribution function (CDF). The hence identified classes of the mapped parameters were displayed as homogeneous areas in the classified parameter maps.

Lineaments are displayed as sharp linear edges on shaded relief surface and show sudden changes in the gamma-dose rates. The final lineament map is a compilation of the manually digitized lineaments on shaded relief surface maps of gamma dose rates. Lineament density gives information (see Fig. 10A) on the local variance of gamma dose rates and it was calculated by the total length of lineaments within a predefined circle of 500 m radius, similar to the dike density map (see Fig. 5) calculation. Length and frequency distribution of lineaments were shown in rose diagrams and compared to those of faults and dikes to see the correlation.

The result maps of digital image processing analysis were compared

to geological maps with special emphasis on dikes and faults using GIS overlay. Spatial modelling was performed with Surfer 10, ILWIS 3.8 and ArcGIS 10 applications.

4. Results and discussion

4.1. Statistical analysis

The summary statistics calculated for the 0 m and 1 m gamma dose rates measured at 300 sites are in Table 2. The average values of gamma dose rate in both heights are in the range of the national average; 58–161 nSv h^{-1} (NERMS, 2014).

Significant relationship between gamma dose rate at 0 m and 1 m height (excluding the outliers) was determined by simple bivariate regression obtaining a linear correlation coefficient (r) 0.98. Similar correlation of gamma dose rates measured at 0 m and 1 m was reported for another area of Hungary with highly different geological background, lower sampling density and with an average sampling distance of 3.2 km by Szabó et al. (2017).

Results of the univariate statistical analysis of 0 m values are shown in Fig. 2A. Ten univariate outliers were identified, in the range of 175–214 nSv h^{-1}, which are located in the southern part of the study area (see Fig. 4A). In all of the identified four bivariate outliers, the 0 m value is higher than 1 m value and all of them are located in the southern part of the study area similarly to univariate outliers (see Fig. 4A). Since one of the aims of this study is to relate the gamma dose rate to the local geology, only the measured gamma dose rate at surface level (0 m) was considered for further analysis.

Geological formations at the study site belong to three different geological periods, Carboniferous (327–290 Ma), Neogene (6–2.4 Ma) and Quaternary (0.13 Ma – present), based on the 1:25,000 scale geological map of the Velence Hills (Figs. 1A and 2B and C) (Gyalog and Horváth, 1999; Horváth et al., 2004). In the map, the Quaternary formations are subdivided in three units, late Pleistocene, late Pleistocene-Holocene and late Holocene times (Fig. 2B).

Box-and-whisker plots of gamma dose rate measured over formations of different geological ages are arranged in the order of decreasing geological age in Fig. 2B. The highest average gamma dose rate value (median 109.3 nSv h^{-1}) belong to late Carboniferous time represented by the prevailing Velence Granite Formation, in the study area (Fig. 2B), including most of the outlying values. Median gamma dose rate value of the Carboniferous time differs from the all of the other ages according to the Mann-Whitney test. However, the gamma dose rates over the Neogene and Quaternary ages do not have statistically significant differences in the median (Fig. 2B). Therefore, the gamma dose rates are not related to the age of the geological formations in the study area. Consequently, age of the geological formations is not a very good indicator for gamma dose rate in this study area.

Box-and-whisker plots of gamma dose rate measured over the different geological formations are arranged first in the order of decreasing geological age and second in the order of decreasing median value (Fig. 2C). Late Carboniferous Velence Granite formation has the highest gamma dose rate median value as it is expected for acidic granitic igneous rocks (UNSCEAR, 2000). Similar results were found in Spain by García-Talavera et al. (2013), where the average gamma dose rate in Paleozoic acid plutonic rock are higher than any kind of Neogene formations. Two types of Velence Granite, biotitic and porphyric
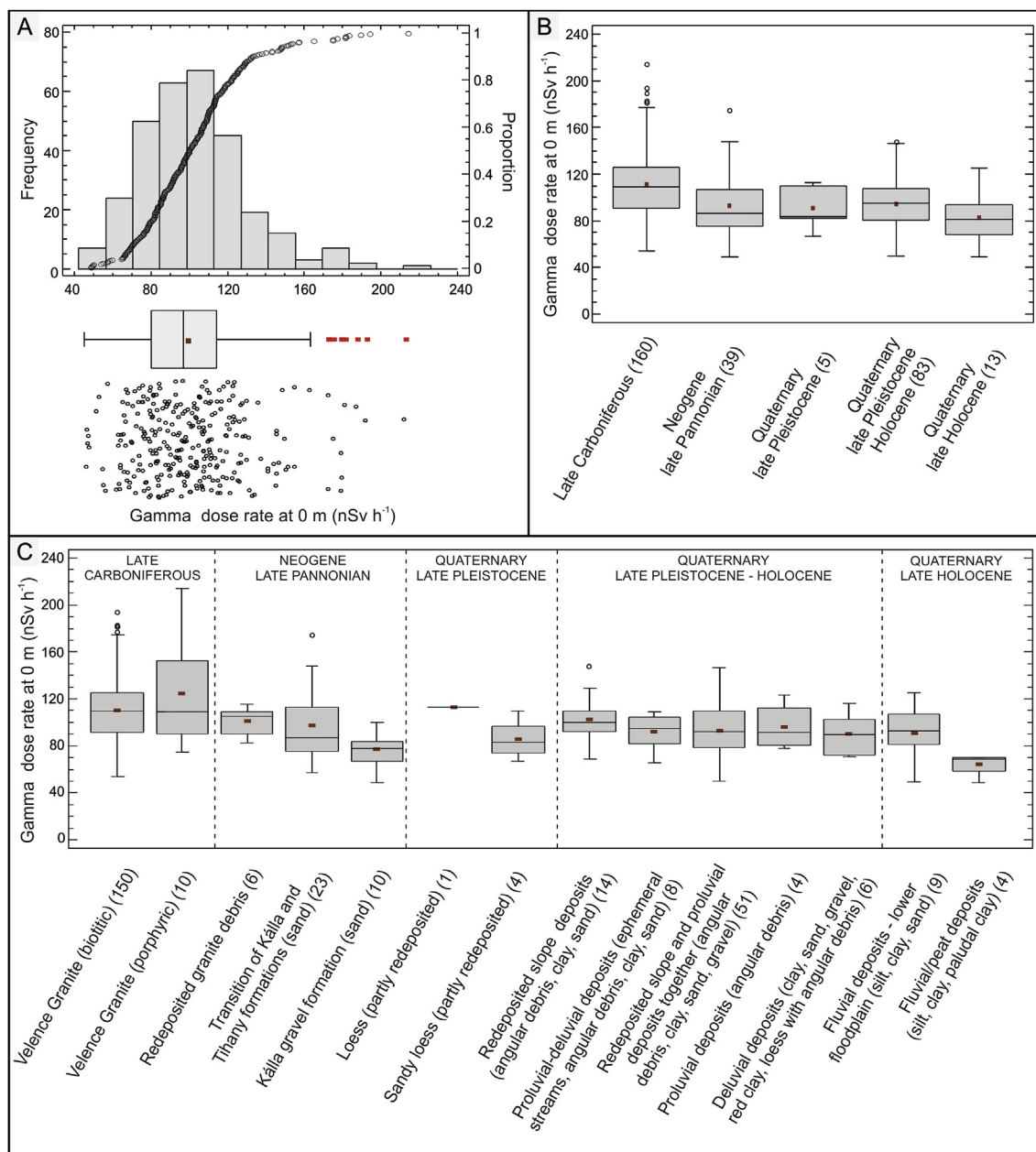
Fig. 2. Statistical analysis of gamma dose rate values measured at surface (0 m) (n = 300). A. Univariate distribution analysis: empirical histogram and cumulative density plot, box-and-whisker plot showing the univariate outliers as solid red dots and scatterplot. B. Box-and-whisker plots of gamma dose rate measured over formations of different geological ages arranged in the order of decreasing geological age. Numbers in the brackets on the X axis are the number of measurement sites. C. Box-and-whisker plots of gamma dose rate measured over different geological formations arranged first in the order of decreasing geological age and second in the order of decreasing median value. Numbers in the brackets on the X axis are the number of measurement sites. (For interpretation of the references to colour in this figure legend, the reader is referred to the Web version of this article.)

ones, distinguished in the geological map (Horváth et al., 2004; Jordan et al., 2018), have the same median gamma dose rate value (109.7 nSv h^{-1} and 109 nSv h^{-1}, respectively, Fig. 2C) based on the Mann-Whitney median homogeneity test. Thus, they can be grouped together from the gamma dose rate point of view. Note that the re-deposited granitic debris of Neogene age derived from the main granitic rocks (Horváth et al., 2004) has similar gamma dose rate value (median 105 nSv h^{-1} based on 6 measurements). However, we cannot state that it is statistically similar to Velence Granite Formation, since the minimum data for the Mann-Whitney median homogeneity test is 9 (Mann and Whitney, 1947). Two other sand formations from the Neo-gene, the Transition of Kálla and Tihany formations and the Kálla gravel formation are similar, having median values of 87.1 nSv h^{-1} and

78 nSv h^{-1}, respectively. Thus, these can be grouped together from gamma dose rate point of view. They are also statistically different in the median from Velence Granite Formation. All of the Quaternary formations, having enough data for the test, are similar statistically.

Simple regression between the measured gamma dose rate and the dike density at each of the 300 measurement sites (Fig. 3A) shows a significant positive correlation (r = 0.34, p = 0.00). This positive cor-relation between gamma dose rate and dike density could be attributed to elevated U and Th concentration of the dikes, which are essantially granite porphyry, compared to the host granite body. Significant posi-tive linear correlation was found between gamma dose rate and its variability index (r = 0.54, p = 0.00). Thus, where the gamma dose rate is high it is also variable, and where it is small it is less variable
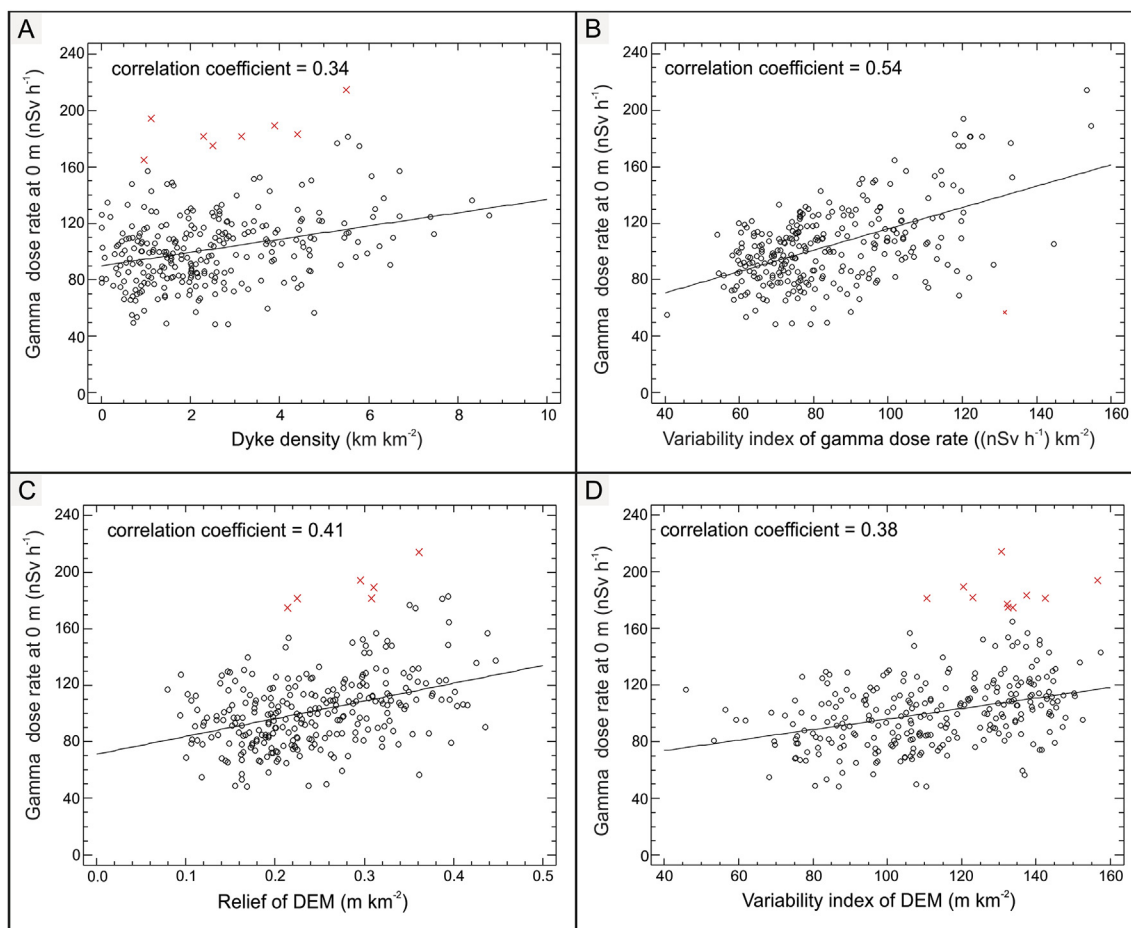
Fig. 3. Bivariate regression analysis. A. Regression between gamma dose rate and dike density. B. Regression between gamma dose rate and its local gamma dose rate variability index. C. Regression between gamma dose rate and the local topographic terrain variability measured by the relief value calculated from the digital elevation model. D. Regression between gamma dose rate and the local topographic terrain variability index value calculated from the digital elevation model. Pearson's linear correlation coefficients are shown in each plot. Red crossed points are bivariate outliers excluded from the regression analysis. See text for details. (For interpretation of the references to colour in this figure legend, the reader is referred to the Web version of this article.)

(Figs. 3B and 4A and B). The correlation coefficient should be viewed with caution, however, as variability index is calculated from the gamma dose rate values and thus it is not an independent variable.

The correlation between the gamma dose rate and the elevation above sea level was evaluated, however no linear correlation was found ($r = 0.16$, $p = 0.0049$). Similar result was found by Szabó et al. (2017). However, there is a significant correlation between the relief and variability index of the topographic elevation (DEM) and the measured gamma dose rates ($r = 0.41$, $p = 0.00$ and $r = 0.38$, $p = 0.00$, respectively) (Fig. 3C and D). Most probably this apparent correlation is induced by the resistance of dikes against weathering, which results in high surface variability, why the chemical composition of the dikes contributes to the high measured gamma dose rates.

4.2. Mapping and spatial analysis

Fig. 4A and B shows the TIN interpolated surface for the gamma dose rate calculated for all data and excluding the outliers, respectively. It can be noticed that all of the univariate outliers and bivariate outliers are located in a SW-NE trending zone in the southern part of the study area (Fig. 4A). The dikes and faults extracted from the 1:25,000 scale geological map of Velence Hills (Horváth et al., 2004; Jordan et al., 2018) are also overlaid to illustrate their location in the high gamma dose rate zones. The high anomalous gamma dose rates have a predominant SW-NE trend and are associated to high fault and dike density zones (Figs. 4B and 5). Despite the high enrichment in U and Th of

monchiquite dikes (Szabó et al., 1993), no anomalies on ambient gamma dose rate were found directly related to these dikes in the study area. It can be explained by the fact that spatially distribution of these three dikes is steep (i.e., subterraneous), therefore their influence on the surface is rather punctual, and their presence was not reflected in the site of the particular sampling grid.

Digital cross-sections (Fig. 4C) were calculated in SW-NE (cross sections: 1, 2, 3) and SE-NW (cross sections: 4, 5, 6) directions, oriented parallel and perpendicular to the orientation of dikes (see Fig. 10), respectively, in order to capture spatial trends. Cross sections 1 and 2 were made in SW-NE orientation along the highest gamma zones (Fig. 4A and C) and they clearly show that gamma dose rates are above the average in these zones (102.5 nSv h^{-1}). It is obviously seen that this area is characterized by granite porphyry dike systems of the same SW-NE orientation. Moreover, high density of dikes characterizes the areas around anomalous high gamma dose rate zones (Fig. 5). Cross-section 3 located entirely in the northwest shows low gamma dose rate values calling attention to heterogeneity in the study area (Fig. 4A and C).

Digital cross sections 5 and 6 drawn in SE-NW orientation show a significant increasing tendency of gamma dose rate towards to south, where the high dike density was revealed (Fig. 5). The dike density map (Fig. 5) shows the highest values (8.86–5.35 km km^{-2}) in the southern part of the study area where high gamma dose rates were also identified (Fig. 4). This was also confirmed by significant linear correlation ($r = 0.34$, $p = 0.00$) between these two parameters described above (Fig. 3A).
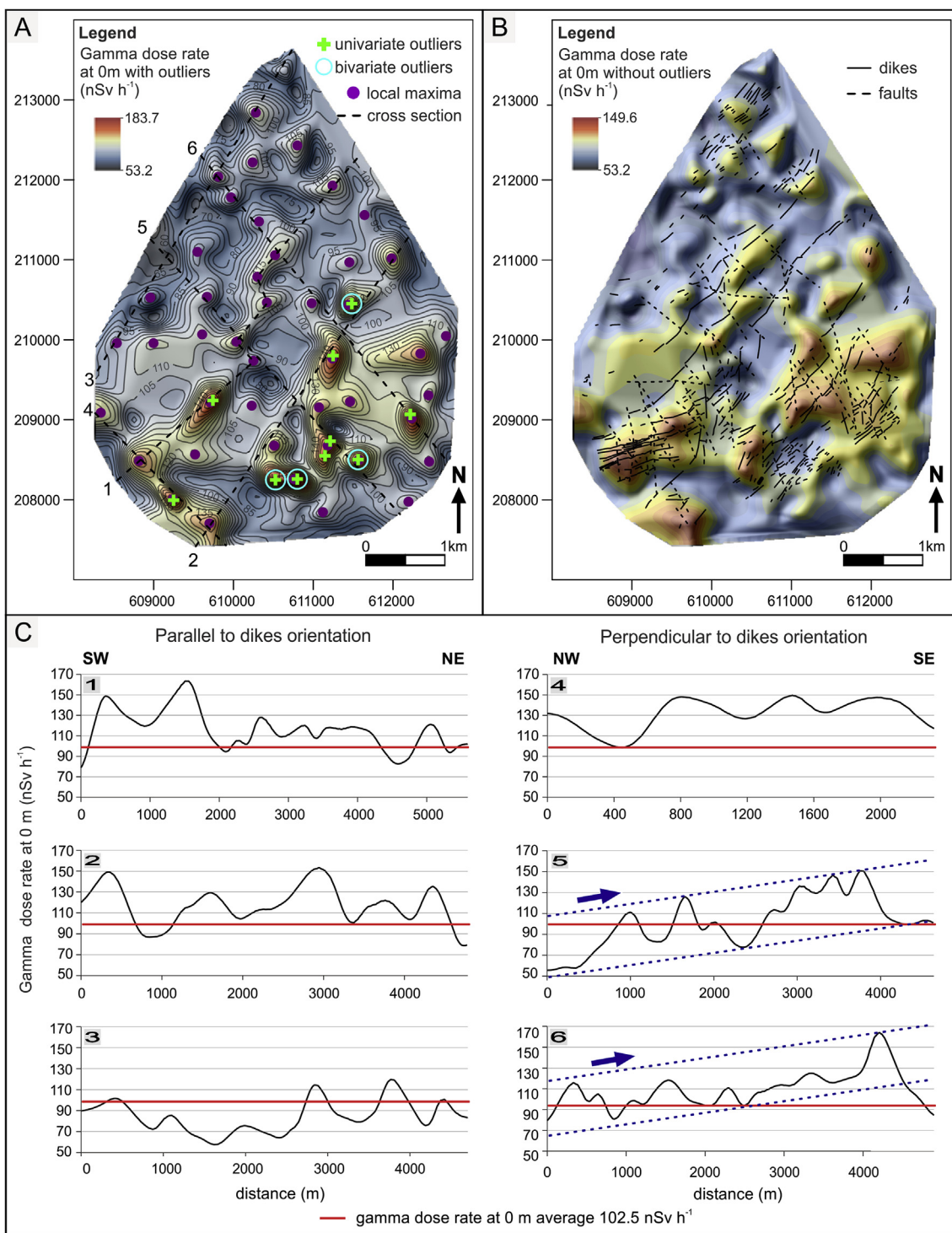
Fig. 4. Triangular irregular interpolation (TIN) based spatial model of gamma dose rates measured at the surface (0 m), smoothed with a 17*17 (170 *170 m) window size moving average low pass filter. A. Composite image of the color coded gamma dose rate map and the shaded relief map calculated from the smoothed TIN model (Guibas and Stolfi, 1985) of the gamma dose rate values. The contour lines are also overlaid. Measured gamma dose rate is in units of nSv h^{-1}. Solid purple dots: local maxima calculated from the smoothed TIN model using the 'higher than algorithm' within a 3 × 3 window size. Light green crosses: statistically identified univariate high outliers (see Fig. 2A). Light blue circles: statistically identified bivariate outliers. Dashed lines show the location of the digital cross-sections (1–6) calculated from the smoothed TIN model and orinted parallel (1–3) and perpendicular (4–6) to the main dike orientation (see Fig. 10). B. The same smoothed TIN model for the gamma dose rate as in Fig. 4A without outliers. Dikes and tectonic fault lines are overlaid. C. Digital cross-sections (1–6) oriented parallel, SW-NE, (1–3) and perpendicular, SE-NW, (4–6) to the main dike orientation (see Fig. 10). Red lines show the average value of the gamma dose rate (102.5 nSv h^{-1}). Blue dased lines and arrows in sections 5 and 6 show the trend of gamma dose rate increasing from NW to SE. Locations of cross-sections are shown in Fig. 4A. (For interpretation of the references to colour in this figure legend, the reader is referred to the Web version of this article.)
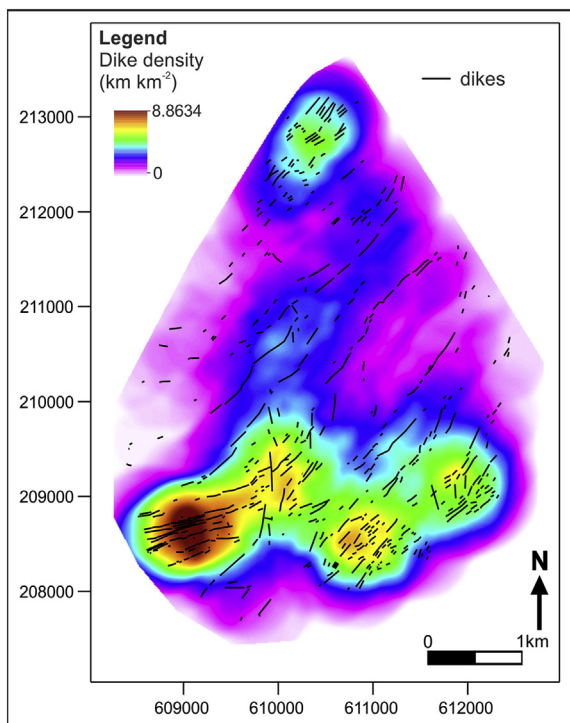
Fig. 5. Dike density map, also showing the dikes (black lines). Note that the highest dike density zones are located in the southern part of the study area.

Local variability of gamma dose rate is represented by relief and variability index parameters, respectively (Fig. 6A and B). High relief (1.31–0.97 ((nSv h^{-1}) km^{-2}) and local variability (155.95–103.17 (nSv h^{-1}) km^{-2}) values were found in the high granite porphyry dike

density zone in the southern part of the study area, southward from about 210000 latitudes (Fig. 5). It was also confirmed by bivariate regression analyses among these variables (r = 0.33, p = 0.00 and r = 0.44, p = 0.00, respectively). The low and high local variability zones follow SW-NE trends and have sharp linear edges in the middle of the study area in parallel to the orientation of the majority of the dikes (Fig. 6A and B). These findings also show that the dikes are related to the measured gamma dose rates spatial distribution.

The spatial autocorrelation of gamma dose rate at 0 m without outliers is represented in the 2D autocorrelogram (Fig. 7A) showing a striking anisotropy in the SW-NE orientation, parallel to the main dikes (see Fig. 10). The directional variograms in SW-NE and the perpendicular directions identify and describe the same anisotropy (Fig. 7B and C).

The direction of the major change in gamma dose rates per distance unit, the gradient direction, is shown in Fig. 8. Grey scale gamma gradient direction map (Fig. 8A) reveals the predominant gradient direction and its spatial location. The orientation was classified in classes of 45° (Fig. 8B) to identify regions with similar gradient direction. The predominant direction (270–360°) marked with blue in the figure has SW-NE trending linear edges, white arrows in Fig. 8, corresponding to the main orientation of dikes (see Fig. 10).

The profile curvature map shows the spatial location of the sudden changes in the gradient magnitude of gamma dose rate (Fig. 9). Negative and positive values correspond to convex ('ridges') and concave ('valleys') zones, respectively (Jordan, 2007). Convex features ('ridges', i.e. positive gamma dose rate anomalies) have SW-NE orientation and they form a left stepping en-echelon pattern. Classified profile curvature map in Fig. 9B enhances the SW-NE oriented linear edges of convex features (emphasised by solid white arrows) which are parallel to the main dike orientation.

The sudden changes in gamma dose rate are represented by the lineaments (Fig. 10A), identified from the shaded relief maps of gamma dose rate (Fig. 4A). The lineament density map shows the spatial
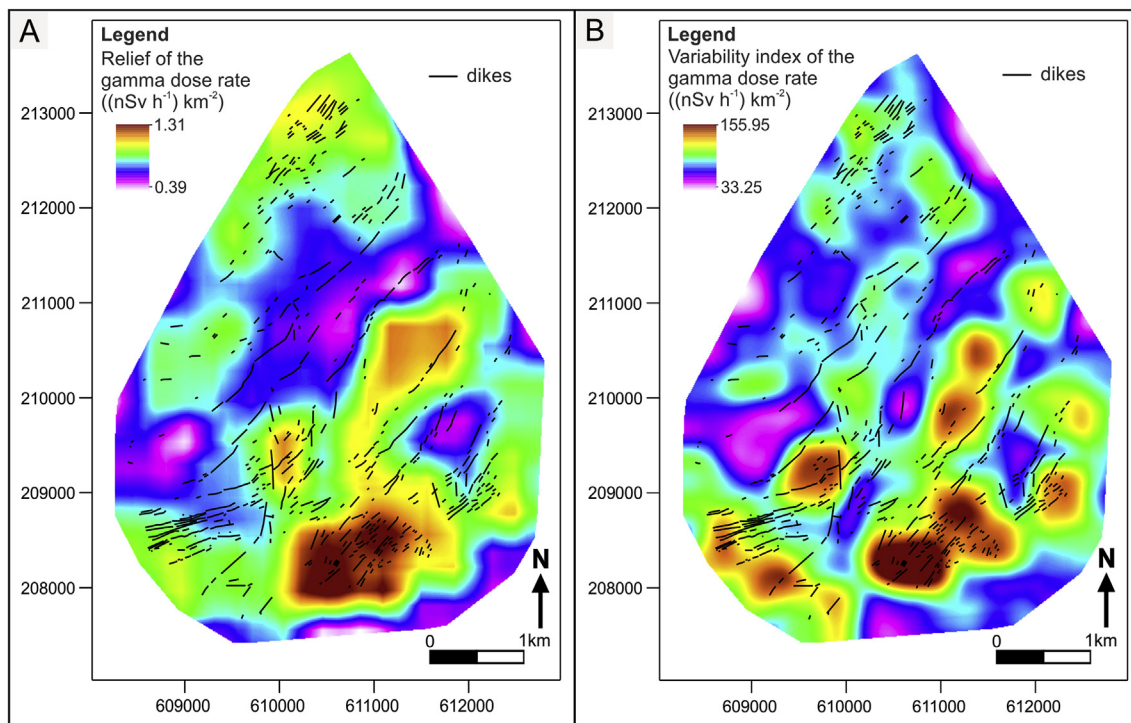

Fig. 6. Local variability analysis for the measured gamma dose rate at the surface (0 m). A. Relief map calculated within a 101 × 101 window size and smoothed with 41 × 41 (410 × 410 m) moving average low pass filter using the outlier free gamma dose rate data. B. Variability index calculated within a 101 × 101 window size and smoothed with 31 × 31 (310 × 310 m) moving average low pass filter from the outlier free data of the measured gamma dose rate. Note that the high relief and variability index (high local variation) values concentrate in the high dike density field in the southern part of the study area.
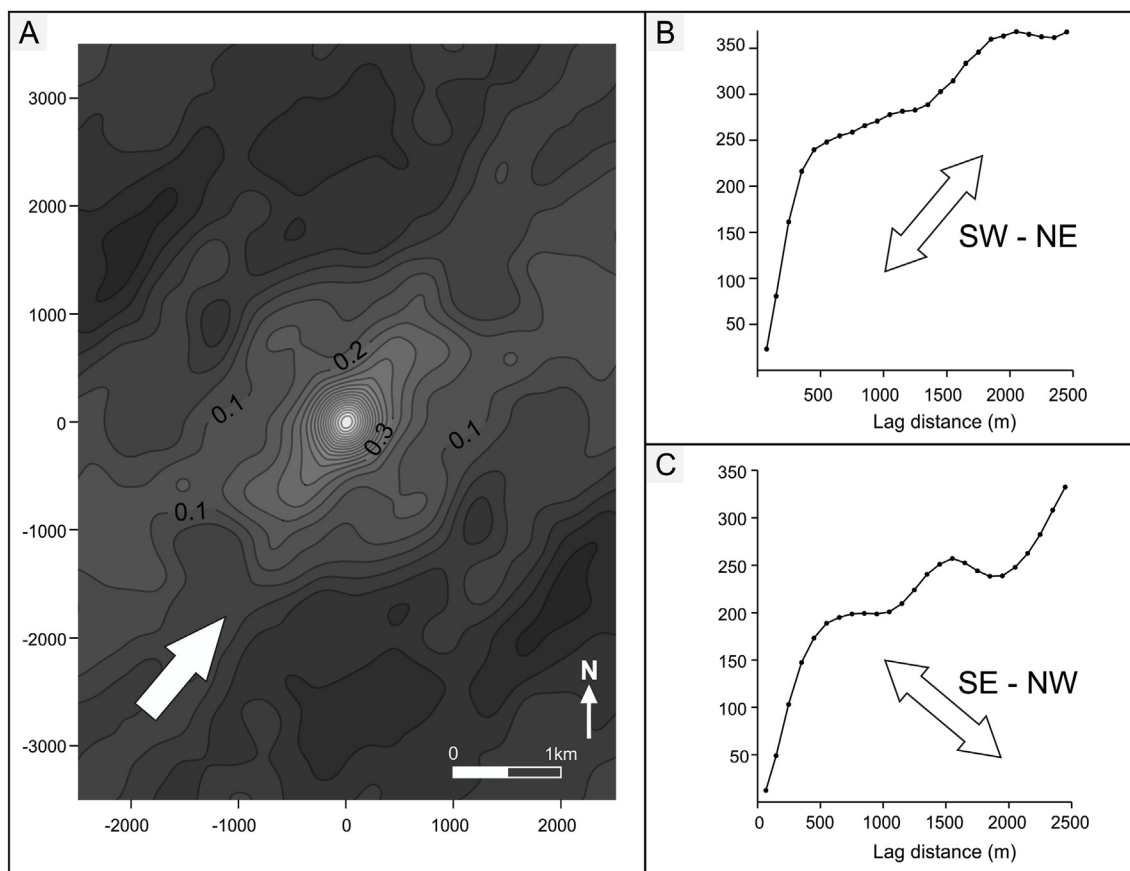
Fig. 7. Spatial autocorrelation analysis for the measured gamma dose rate at the surface (0 m). A. 2D autocorrelogram for the gamma dose rate calculated from the smoothed TIN model. Contour lines show Pearson's correlation coefficient. Note the strong SW-NE anisotropy parallel to the main dike orientation (see Fig. 10), emphasised by the solid white arrow. Coordinates are in meters. B. Directional variogram calculated from the smoothed TIN model in the SW-NE direction parallel to the main dike orientation (azimuth 60°, tolerance 30°). C. Directional variogram calculated from the smoothed TIN model in the SE-NW direction parallel to the major fault lines and perpendicular to main dike orientation (azimuth 150°, tolerance 30°).

distribution of the lineaments in the study area. The highest total length of lineaments per unit area can be found in the southern part (Fig. 10A), where the highest variability and dike density were also identified (Figs. 5 and 6). Frequency and length based rose diagrams of lineaments (Fig. 10B) reveal two main orientations: SW-NE and SE-NW. Similar evaluation was performed on the orientation of faults and dikes of the study area extracted from the 1:25,000 scale geological map of Velence Hills (Horváth et al., 2004, Fig. 1B). The main orientation of faults is SE-NW, whereas the main orientation of dikes is SW-NE (Fig. 10C), which corresponds to the extensive structural measurements on granite porphyry and quarz dikes and joints made by Benkó et al. (2014) in Velence Hills (Fig. 10D). Concluding, the gamma dose rate sudden changes represented by lineaments have the same directions as the faults and granite prophyre dikes. The N-S and E-W directions in the rose diagram cannot be explained at this point of the research.

5. Conclusions

This study has two main findings: 1) the high gamma dose rate anomaly, also characterized by high variability, spatially coincides with the high dike density area, and 2) the two main lineament directions (NE-SW and NW-SE) identified in the gamma dose rate coincide with the prevailing orientations of the underlying granitic dikes and fractures.

Thus, this study confirms that the main spatial features identified in the gamma dose rate map are influenced by the underlying geological setting such as rock litholugy, dike system and fault network arrangement in the study area. Significant positive linear correlation was found

between the measured gamma dose rate and the dike density. The simple digital cross-section analysis proved to be efficient in describing spatial trends, whereas the more advanced procedures of gradient (slope, aspect, curvature) calculations identified the prevailing orientations in the SW-NE and SE-NW directions as significant linear edges (lineaments) of gamma dose rates in the study area. Anisotropy along these orientations was characterized by autocorrelation and directional variogram calculations. The relief and local variability index identified areas of anomalous high local variability of the gamma dose rate coinciding with the area of high dike density in the southern part of the study area. This statement was also confirmed by their significant positive correlation. The locations of high variability are also the areas where gamma dose rates are the least predictable. The circular statistics calculated from the lineament map revealed two major directions corresponding to geological settings such as the dike system and fault zones.

Our study has shown that digital spatial analysis methods, including digital image processing techniques, are efficient in revealing spatial pattern in gamma dose rates and in identifying the relationship between the spatial pattern and the underlying geological setting at high resolution local scale, having 300 measurement sites in an about 4 × 5 km area with a 250 m sampling distance. It is concluded that these methods provide useful means for the recognition and characterization of spatial pattern in field measured ambient gamma dose equivalent rate at the local scale, too.
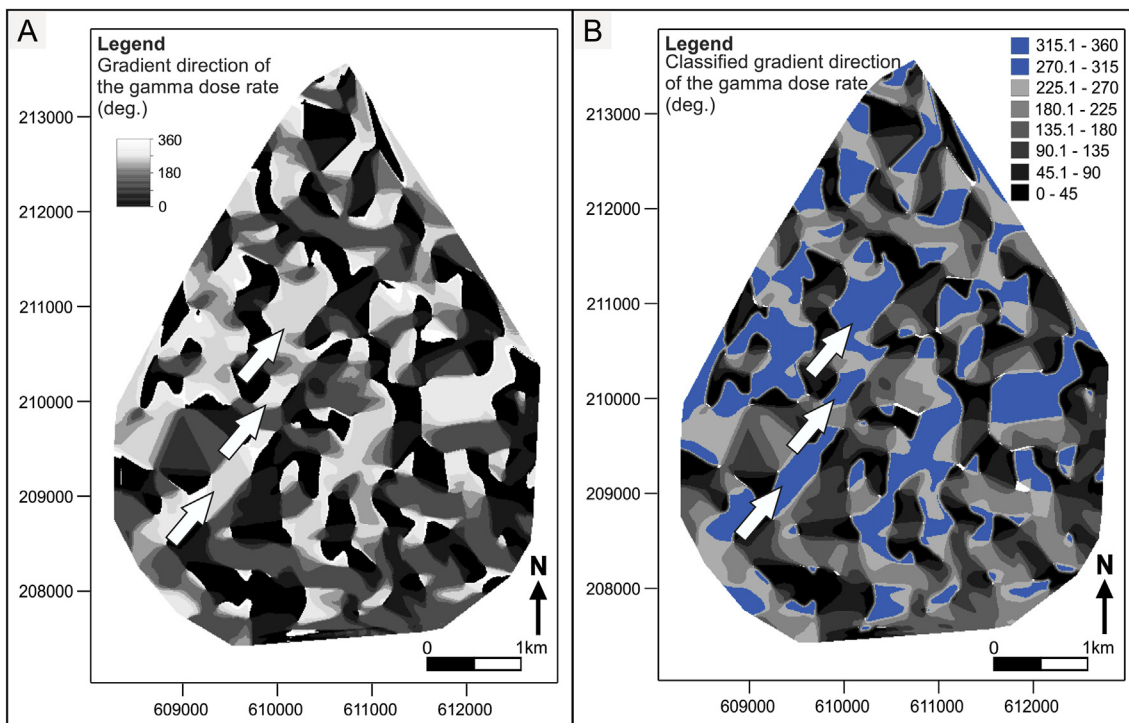
Fig. 8. Gradient direction analysis of the gamma dose rate measured at the surface (0 m). A. Gradient direction map in grey scale shading. B. Classified gradient direction map in classes of 45°. Note the SW-NE oriented linear edges (indicated by solid white arrows) of the dominant gradient direction, (emphasised by blue shading), which are parallel to the main dike orientation. The zero degree (0°) direction is to the North. (For interpretation of the references to colour in this figure legend, the reader is referred to the Web version of this article.)
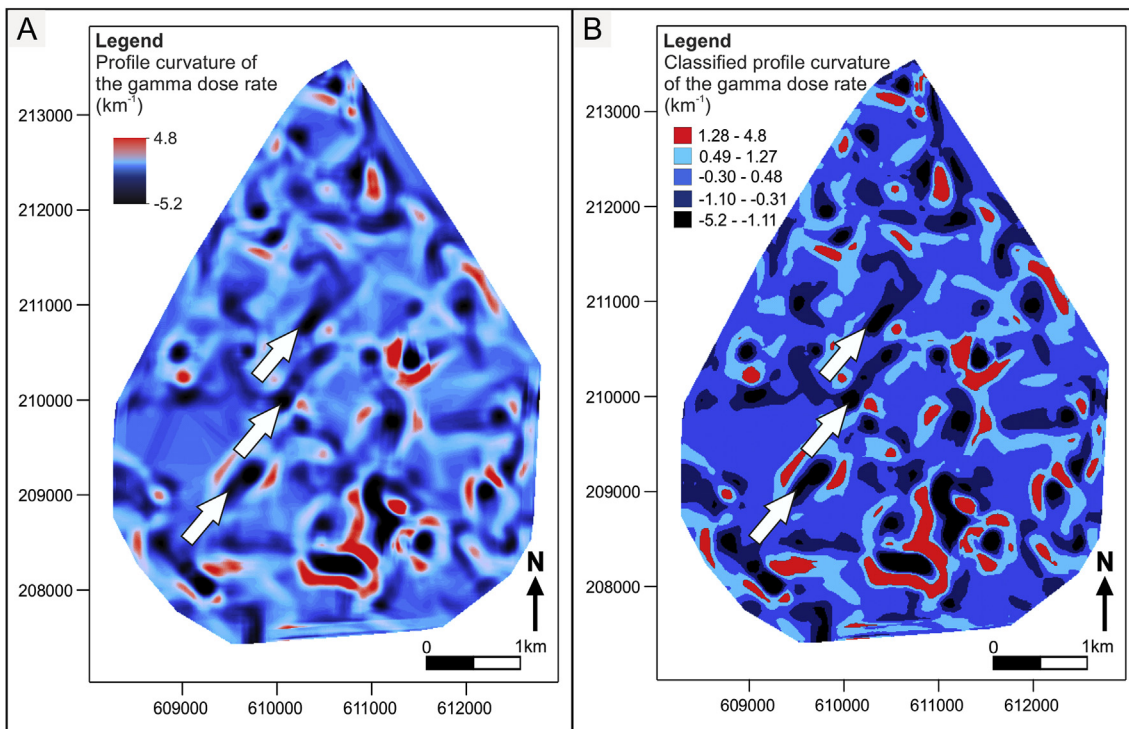
Fig. 9. Profile curvature analysis for the measured gamma dose rate at the surface (0 m). A. Color scale profile curvature map. B. Classified profile curvature map. Note the SW-NE oriented linear edges of the dominant profile curvature direction, indicated by solid white arrows, which are parallel to the main dike orientation. Positive and negative values are concave and convex surface points, respectively. (For interpretation of the references to colour in this figure legend, the reader is referred to the Web version of this article.)
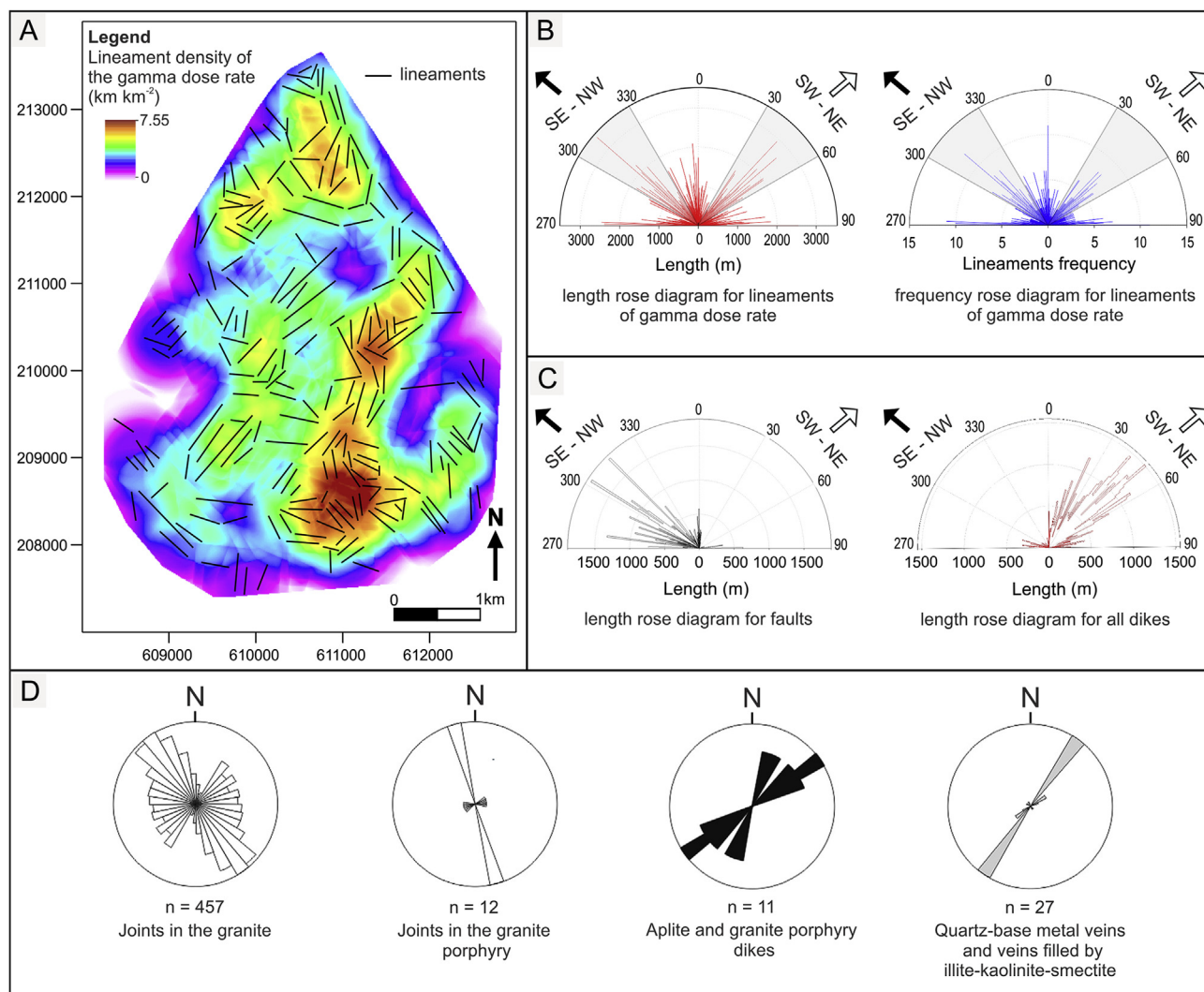
Fig. 10. Lineament analysis for the measured gamma dose rate at the surface (0 m). A. Color scale lineament density map of gamma dose rate identified manually on eight shaded relief maps of gamma dose rate. Lineaments (black lines) are also shown. B. Length and frequency rose diagrams for the measured gamma dose rate lineaments. Grey shading indicates the dispersion of the two main orientations of the gamma dose rate lineaments: SE-NW and SW-NE indicated by black and white arrows, respectively. C. Length rose diagram for all types of dikes and faults, extracted from the 1:25,000 scale geological map of the Velence Hills (Horváth et al., 2004); see Fig. 1B). Note the main orientation of the dikes and faults are similar to the gamma dose rate lineament main orientations (SW-NE and SE-NW), indicated by the corresponding white and black arrows. D. Orientation of dikes, hydrothermal veins and joints in the studied area according to Benkó et al. (2014). The number (n) of joints and dikes studied in the field are shown. (For interpretation of the references to colour in this figure legend, the reader is referred to the Web version of this article.)

References

Benkó, Z., Molnár, F., Lespinasse, M., Váczi, T., 2014. Evidence for exhumation of a granite intrusion in a regional extensional stress regime based on coupled microstructural and fluid inclusion plane studies - an example from the Velence Mts. Hungary. J. Struct. Geol. 65, 44–58.

Bossew, P., Cinelli, G., Cernohlawek, N., Gruber, V., Friedmann, H., Dehandschutter, B., Menneson, F., Garcia-Talavera, M., Da Silva, N., Tollefsen, T., Nishev, A., Hernandez-Ceballos, M.A., de Cort, M., 2015a. Can ambient dose rate be used for predicting the geogenic Rn Potential? Presentation. In: Conference Radon in the Environment, Krakow (Poland), 26–29 May 2015, . http://radon.ifj.edu.pl/eng/htdocs/main.php?cĽradon_2015, Accessed date: 21 January 2015.

Bossew, P., Cinelli, C.G., Cernohlawek, N., Gruber, V., Menneson, V., Tollefsen, T., Nishev, A., Hernandez-Ceballos, M.A., de Cort, M., 2015b. Can terrestrial gamma dose rate serve as predictor of geogenic radon. Presentation. In: Conference Rad-2015, Budva (Montenegro), 8–12 June 2015, . http://www.rad2015.radconference.org/news.php, Accessed date: 5 February 2016 section radon-thoron.

Bossew, P., Cinelli, G., Hernández-Ceballos, M., Cernohlawek, N., Gruber, V., Dehandschutter, B., Menneson, F., Bleher, M., Stöhlker, U., Hellmann, I., Weiler, F., Tollefsen, T., Tognoli, P.V., de Cort, M., 2017. Estimating the terrestrial gamma dose rate by decomposition of the ambient dose equivalent rate. J. Environ. Radioact. 166, 296–308.

Buda, G., 1981. Genesis of the Hungarian granitoid rocks. Acta Geol. Acad. Sci. Hung. 24, 309–318.

Burján, Z., Nagy-Balogh, J., Gál-Sólymos, K., Szabó, C.S., 2002. Spectrochemical study of potential source minerals of radon anomaly. Microchem. J. 73, 47–51.

Burrough, P.A., 1986. Principles of Geographical Information Systems for Land Resources Assessment. Clarendon Press, Oxford (Chapter 3): Digital Elevation Models.

Cinelli, G., Tollefsen, T., Bossew, P., Gruber, V., De Cort, M., 2015. The european atlas of natural radiation. In: Presentation, Conference Rad-2015, Budva (Montenegro), 8–12

June 2015, . http://www.rad2015.rad-conference.org/news.php, Accessed date: 5 February 2016 section radon-thoron.

Davis, J.C., 2011. Statistics and Data Analysis in Geology. J. Wiley & Sons, India.

De Cort, M., Gruber, V., Tollefsen, T., Bossew, P., Janssens, A., 2011. Towards a European atlas of natural radiation: goal, status and future perspectives. Radioprotection 46, 737–743.

Drury, S.A., 1987. Image Interpretation in Geology. Allen and Unwin, London, UK.

Evans, I.S., 1972. General geomorphometry, derivatives of altitude, and descriptive statistics. In: Chorley, R.J. (Ed.), Spatial Analysis in Geomorphology. Methuen, London, pp. 17–90.

Garbrecht, J., Martz, L.W., 1995. Agricultural research service publication NAWQL 95-3. In: TOPAZ: an Automated Digital Landscape Analysis Tool for Topographic Evaluation, Drainage Identification, Watershed Segmentation and Subcatchment Parameterisation: TOPAZ User Manual. U.S. Department of Agriculture.

García-Talavera, M., García-Pérez, A., Rey, C., Ramos, L., 2013. Mapping radon-prone areas using γ-radiation dose rate and geological information. J. Radiol. Prot. 33, 605–620.

Gonzalez, R.C., Woods, R.E., 1993. Digital Image Processing Third Edition. Pearson Prentice Hall, Upper Saddle River.

Guibas, L., Stolfi, J., 1985. Primitives for the manipulation of general subdivisions and the computation of Voronoi diagrams. ACM T. Graphic 4, 74–123.

Gyalog, L., Horváth, I., 1999. Geological Map of the Velence hills. Geological Institute of Hungary, Budapest.

Hiemstra, P.H., Pebesma, E.J., Twenhöfel, C.J.W., Heuvelink, G.B.M., 2009. Real-time automatic interpolation of ambient gamma dose rates from the Dutch radioactivity monitoring network. Comput. Geosci. 35, 1711–1721.

Horváth, I., Daridáné Tichy, M., Dudko, A., Gyalog, L., Ódor, L., 2004. Geology of the Velence Hills and the Balatonfő. Geological Institute of Hungary, Budapest.

ICRU 51, September 1993. Commission on Radiation Units and Measurements: Quantities and Units in Radiation protection Dosimetry. Report 51(1). Intl. .

Jordan, G., Meijninger, B.M.L., van Hinsbergen, D.J.J., Meulenkamp, J.E., van Dijk, P.M., 2005. Extraction of morphotectonic features from DEMs: development and applications for study areas in Hungary and NW Greece. Int. J. Appl. Earth Obs 7, 163–182.

Jordan, G., 2007. Digital terrain analysis in a GIS environment. Concepts and development. In: Peckham, R.J., Jordan, G. (Eds.), Digital Terrain Modelling, Development and Applications in a Policy Support Environment. Springer Verlag, Berlin, pp. 2–39.

Jordan, G., Petrik, A., De Vivo, B., Albanese, S., Demetriades, A., Sadeghid, M., the GEMAS Project Team, 2018. GEMAS: spatial analysis of the Ni distribution on a continental-scale using digital image processing techniques on European agricultural soil data. J. Geochem. Explor. 186, 143–157.

Mann, H.B., Whitney, D.R., 1947. On a test of whether one of two random variables is stochastically larger than the other. Ann. Math. Stat. 18, 50–60.

Manohar, S.N., Meijer, H.A.J., Herber, M.A., 2013. Radon flux maps for The Netherlands and Europe using terrestrial gamma radiation derived from soil radionuclides. Atmos. Environ. 81, 399–412.

Mezősi, G., 2015. Granite weathering in the velence hills. In: Lóczy, D. (Ed.), Landscapes and Landforms of Hungary. World Geomorphological Landscapes. Springer, pp. 89–95 Cham.11.

NERMS, 2014. OKSER 2013. Annual Report of the National Environmental Radiological Monitoring System. pp. 86.

Quindós, L.S., Fernández, P.L., Sainz, C., Fuente, I., Nicolás, J., Quindós, L., Arteche, J., 2008. Indoor radon in a Spanish region with different gamma exposure levels. J. Environ. Radioact. 99, 1544–1547.

Ramli, A.T., Abdel Wahab, M.A., Lee, M.H., 2001. Geological influence on terrestrial gamma ray dose rate in the Malaysian state of Johore. Appl. Radiat. Isot. 54, 327–333.

Rodgers, J.L., Nicewander, W.A., 1988. Thirteen ways to look at the correlation coefficient. Am. Statistician 42, 59–66.

Sanusi, M.S.M., Ramli, A.T., Gabdo, Garba N.N., Heryanshah, A., Wagiran, H., Said, M.N., 2014. Isodose mapping of terrestrial gamma radiation dose rate of Selangor state, Kuala Lumpur and Putrajaya, Malaysia. J. Environ. Radioact. 135, 67–74.

Szabó, C.S., Kubovics, I., Molnár, Zs, 1993. Alkaline lamprophyre and related dyke rocks in NE Transdanubia, Hungary: the Alcsutdoboz-2 (AD-2) borehole. Mineral. Petrol. Times 47, 127–148.

Szabó, K.Z., Jordan, G., Horváth, Á., Szabó, C., 2014. Mapping the geogenic radon potential: methodology and spatial and spatial analysis for central Hungary. J. Environ. Radioact. 129, 107–120.

Szabó, K.Z., Jordan, G., Petrik, A., Horváth, Á., Szabó, C., 2017. Spatial analysis of ambient gamma dose equivalent rate data by means of digital image processing techniques. J. Environ. Radioact. 166, 309–320.

Szegvary, T., Conen, F., Stöhlker, U., Dubois, G., Bossew, P., de Vries, G., 2007. Mapping terrestrial γ-dose rate in Europe based on routine monitoring data. Radiat. Meas. 42, 1561–1572.

Takahashi, S., Ikeda, T., Shinagawa, Y., Kunii, T.L., Ueda, M., 1995. Algorithms for extracting correct critical points and constructing topological graphs from discrete geographical elevation data. Comput. Graph. Forum 14, 181–192.

Tukey, J.W., 1977. Exploratory Data Analysis. Addison-Wesley.

UNSCEAR, 2000. Sources and effects of ionizing radiation. In: Sources, Annex B, vol. II United Nations, New York).

Yeşilkanat, C.M., Kobya, Y., Taşkin, H., Çevik, U., 2015. Dose rate estimates and spatial interpolation maps of outdoor gamma dose rate with geostatistical methods; A case study from Artvin, Turkey. J. Environ. Radioact. 150, 132–144.